European Journal of Mechanics / B Fluids 120 (2026) 204569

Contents lists available at ScienceDirect

European Journal of Mechanics / B Fluids

journal homepage: www.elsevier.com/locate/ejmflu

Non-equilibrium transport dynamics and macroscopic thermodynamic efficiency of binary Knudsen flow in tapered semipermeable channels

Antonio F. Miguel [a,b,*]

[a] University of Evora, School of Sciences and Technology, Department of Physics, Rua Romao Ramalho 59, Evora 7000-761, Portugal
[b] Complex Flow Systems Lab, ICT, Apartado 94, Evora 7002-554, Portugal

ARTICLE INFO

Keywords:
Knudsen flow
Non-equilibrium thermodynamics
Entropy generation
Geometric optimization
Membrane gas separation

ABSTRACT

This study investigates the non-equilibrium transport dynamics and macroscopic thermodynamic efficiency of a binary gas mixture traversing a tapering, selectively permeable cascade operating strictly within the Knudsen regime. By employing a Lagrangian test particle Monte Carlo framework alongside a Fokker-Planck formalism, discrete stochastic trajectories driven by particle-boundary interactions are coupled with ensemble macroscopic concentration profiles. The separation process is thermodynamically evaluated by balancing the separation work gain against two primary costs: the microscopic entropic penalty of momentum erasure via diffuse wall collisions, and the macroscopic transport penalty induced by geometric backscattering. To formalize this, the specific separation thermodynamic efficiency is introduced, a metric that normalizes overall performance against the intrinsic material transmission probability. The results reveal a critical morphological transition in optimal cascade architecture. It is demonstrated that low-affinity membranes fundamentally require moderate geometric constriction to mechanically force boundary collisions and maximize the integrated probability of permeation, optimally balancing permeation against induced backscattering. On the other hand, in high-affinity systems, the active species is rapidly extracted near the inlet, localizing maximum thermodynamic dissipation and rendering severe tapering physically detrimental. Consequently, highly selective membranes strictly favor uniform channel geometries to mitigate irreversible transport losses. Finally, this framework establishes that optimal geometric design is not static but must be dynamically tailored to the intrinsic surface affinity to maximize macroscopic thermodynamic efficiency.

1. Introduction

Driven by the stringent thermodynamic limits of high-purity molecular separation, the non-equilibrium transport of rarefied gases through nanoconfined geometries has emerged as a critical frontier in modern statistical physics [1,2]. When the molecular mean free path significantly exceeds the characteristic transverse scale of the confining channel, the system enters the free-molecular or Knudsen flow regime [3,4]. In this limit, intermolecular scattering becomes negligible, and the transport dynamics are dictated entirely by stochastic particle-boundary interactions, typically governed by the laws of diffuse reflection [5–7].

The utility of Knudsen diffusion spans a broad technological spectrum, underpinning critical processes such as molecular sieving in highly selective carbon and zeolite membranes [8], isotopic fractionation in uranium enrichment cascades [9], and the extraction dynamics of shale gas within nanoporous geological formations [10,11]. Beyond these engineering frontiers, Knudsen transport serves as a foundational paradigm in theoretical physics for probing the limits of non-equilibrium statistical mechanics and anomalous transport [12]. At the intersection of these domains lies the fundamental challenge of binary gas separation [13]. This process is rigorously modeled as a differential interaction between species and a selective boundary. While the inert component is restricted by an impervious, diffusely reflecting wall, the targeted species possesses a finite transmission probability, effectively transforming the boundary into a stochastic mass sink [14,15].

To augment the separation efficiency of these selectively permeable systems, geometric modulation of the transport channel is frequently employed [16]. While uniform nanopores provide a standard analytical baseline, tapered and cascaded geometries introduce a broken spatial symmetry that functions as a physical concentrator [17]. By imposing a

* Corresponding author at: University of Evora, School of Sciences and Technology, Department of Physics, Rua Romao Ramalho 59, Evora 7000-761, Portugal.
E-mail address: afm@uevora.pt.

https://doi.org/10.1016/j.euromechflu.2026.204569
Received 27 February 2026; Received in revised form 26 April 2026; Accepted 31 May 2026
Available online 2 June 2026

longitudinal reduction in channel width, tapering forces a localized acceleration of the collision frequency, thereby maximizing the integrated probability of permeation for low-affinity species [18]. However, this geometric constriction simultaneously introduces severe macroscopic transport penalties, suppressing the forward throughput and dramatically shifting the spatial distribution of permeation hotspots [19]. Consequently, the efficacy of such geometric modifications cannot be universally generalized. It is strictly coupled to the intrinsic surface affinity of the selective boundary. While severe tapering may be fundamentally required to force particle-wall interactions in low-permeability systems, it threatens to introduce unrecoverable parasitic transport losses in high-affinity membranes where intrinsic permeation is already highly efficient.

The optimization of these tapered geometries cannot be evaluated purely through mass transport metrics, it requires a rigorous thermodynamic accounting of irreversibility. Local entropy production [20] provides a continuous mesoscopic field description of the thermodynamic costs associated with frictional backscattering and the dissipation of concentration gradients. Furthermore, because highly selective membranes operate at the nexus of macroscopic thermodynamic forces and microscopic stochasticity, establishing the absolute bounds of separation requires framing the transport dynamics within the context of fluctuation theorems [21,22]. By extending classical non-equilibrium thermodynamics to finite-time microscopic trajectories, this formalism imposes exact symmetries on the probability distribution of entropy production [23]. Rather than necessitating the explicit numerical resolution of rare, non-Gaussian stochastic events (such as particles transiently moving against chemical gradients), this framework serves as a fundamental theoretical constraint. It ensures that the localized thermodynamic costs of permeation are rigorously accounted for, thereby dictating the maximum achievable separation factors and guaranteeing that any macroscopic geometric optimization inherently respects the deep statistical mechanical limits of the open system [24].

While extensive literature has established the kinetic foundations of rarefied gas flow and optimized transport within complex pore networks, the explicit thermodynamic optimization of tapered geometries for binary gas separation remains underexplored. Historically, the evaluation of selectively permeable systems has predominantly relied on bulk macroscopic mass-transport metrics [25,26], or has been analytically restricted to geometrically uniform cylindrical baselines [27–29]. While these prior studies, spanning classical continuum models to very recent literature, provide critical phenomenological insights, they largely decouple the structural architecture from the localized, discrete thermodynamic costs of transport. In this paper, this gap is addressed by extending previous stochastic modeling efforts to evaluate tapered Knudsen channels featuring selectively permeable boundaries. The fundamental novelty of the present study lies in explicitly coupling broken spatial symmetry (longitudinal tapering) directly with a microscopic, fluctuation-theorem-based entropy model. By formalizing this coupling through a Lagrangian ballistic trajectory solver, the fundamental trade-off between geometric collision forcing and parasitic macroscopic backscattering is quantified. Consequently, the proposed framework frames physical geometry not merely as a passive boundary condition for flow rectification, but as an active thermodynamic variable that dictates the microscopic entropic cost of momentum erasure. Furthermore, a specific separation thermodynamic efficiency metric is introduced to decouple geometric flow resistance from intrinsic membrane chemistry. Conceptually, this metric acts as the primary objective function for cascade design. It is formulated to normalize the macroscopic thermodynamic utility (the separation work gain) against the dual penalties of microscopic momentum erasure (frictional entropy generation) and macroscopic geometric resistance (inlet backscattering). Through this framework, the potential for a critical morphological transition in optimal channel architecture is examined as a function of the intrinsic surface affinity of the boundary. This approach provides a unified methodology to identify the geometric configurations that maximize separation performance while rigorously adhering to the thermodynamic limits of over-constricted flows. This manuscript is organized as follows. Section 2 establishes the model, detailing the stochastic dynamics of Knudsen transport, the derivation of localized entropy production from fluctuation theorems, and the formalization of the macroscopic thermodynamic efficiency metrics. Section 3 outlines the computational methodology, defining the custom Test Particle Monte Carlo solver utilized to simulate the stochastic boundary interactions and reconstruct the macroscopic probability fields. Section 4 presents the results and discussion, evaluating the coupled effects of geometric tapering and intrinsic surface affinity on both the localized transport dynamics and the global separation efficiency. Finally, Section 5 summarizes the core findings and concludes the study.

2. Model

2.1. Stochastic dynamics and macroscopic transport in Knudsen flow

To model the transport dynamics, the physical domain is defined as a high-aspect-ratio conduit aligned along the z-axis, characterized by a length L and transverse dimension d, containing a binary mixture of species A and B. Operation is considered strictly within the Knudsen regime (Kn=l/d>>1 where l is the mean free path). Under these conditions, intermolecular scattering is suppressed, and the dynamics are dominated entirely by particle-boundary interactions. Assuming thermalized, rough boundaries, reflection is governed by the Knudsen cosine law, which effectively randomizes the momentum vector following each collision. This rapid thermalization permits the neglect of inertial effects in favor of the damping induced by wall collisions, justifying the adoption of an overdamped Langevin formalism.

The instantaneous microstate of the system $\Gamma(t)=z_1(t) + z_2(t) + \ldots z_N(t)$, where z_k represents the axial position of the k^{th} particle within the channel, is defined by the axial positions of all N particles. The stochastic trajectory of a single particle k of species i, where $i \in \{A, B\}$, is governed by the Langevin equation

$$\gamma_i \dot{z}_k(t) = -\frac{\partial U(z_k)}{\partial z_k} + f_k(t) + \xi_k(t) \quad (1)$$

where γ_i is friction coefficient for species i, $U(z_k)$ is the potential energy landscape, and $f_k(t)$ represents any non-conservative external forces driving the flow such as a pressure gradient. The term $\xi_k(t)$ represents Gaussian white noise characterizing thermal fluctuations. This noise satisfies the fluctuation-dissipation theorem, $\langle\ \xi_k(t)\ \xi_l(t')\ \rangle = 2k_BT\ \gamma_i\delta_{kl}\delta(t-t')$, where k_B is the Boltzmann constant, ensuring the system relaxes to equilibrium at temperature T in the absence of driving forces.

On timescales t significantly exceeding the ballistic flight time, this longitudinal motion coarse-grains into a diffusive process via the central limit theorem [30]. The trajectory is thus equivalently described by the Knudsen diffusion coefficient, derived from kinetic theory as $D_K^i = \frac{1}{4}d\bar{v}_i$, where the mean thermal velocity is $\bar{v}_i = \sqrt{\frac{8k_BT}{\pi m_i}}$. The drift velocity $v_d^i(z) = \beta D_K^i f_i$ arises from thermodynamic force $f_i = -\nabla\mu_i$ where $\beta = 1/k_BT$ and μ refers to the chemical potential.

To formalize the separation efficiency, the analysis is bifurcated into two distinct boundary conditions. The first is a strictly reflective system where hard-wall boundaries ensure particle conservation. The second is a semipermeable architecture where the walls interact selectively with the mixture. In this latter scenario, the non-permeating species is confined by reflective Neumann conditions, while the permeating species undergoes stochastic absorption governed by the wall's transmission probability. Transitioning from discrete trajectories to ensemble behavior, the Fokker-Planck equation is employed to describe the time evolution of the macroscopic concentration profile. For the impervious channel, probability mass is strictly conserved, obeying the continuity equation in configuration space

$$\frac{\partial P(\Gamma,t)}{\partial t} = -\sum_{k=1}^{N}\frac{\partial}{\partial z_k}J_k(\Gamma,t) \tag{2}$$

where P(Γ,t) is the joint probability density, and J_k is the probability current for the k^{th} particle

$$J_k\left(\Gamma,t\right) = \frac{1}{\gamma_i}\left[\left(-\frac{\partial U}{\partial z_k}+f_k\right)P\left(\Gamma,t\right)-k_BT\frac{\partial P(\Gamma,t)}{\partial z_k}\right] \tag{3}$$

that represents the competition between drift and diffusive spreading. Macroscopically, under steady-state conditions with fixed reservoir boundaries, this zero-divergence flux yields a linear density profile $\rho_A(z)\propto(L\text{-}z)$, where the thermodynamic force is uniformly distributed to overcome frictional resistance.

For the selectively permeable system, the symmetry between species is broken, transforming the domain into a grand canonical open system where particle number fluctuations drive the dynamics. The Fokker-Planck formulation for the permeable species acquires a sink term representing the transverse flux extraction

$$\frac{\partial P_{perm}(z,t)}{\partial t} = -\nabla.J_{perm}(z,t)-k_{leak}(z)P_{perm}(z,t) \tag{4}$$

Here, $k_{leak}(z)$ is a localized rate function proportional to the thermal velocity and transmission probability, scaling as $\Gamma_{perm}(z) \sim 4P_{perm}/d$. This fundamentally alters the macroscopic observable, transforming the steady-state density into a reaction-diffusion profile exhibiting exponential decay, $\rho_{perm}(z) \propto \exp[-z\Gamma_{perm}(z)]$. Physically, this decay length signifies that the majority of the permeating species is extracted near the inlet. Notice that, while the confined species is nominally conserved, its dynamics are coupled to the leaking species. As the permeating particles escape, the effective collision landscape shifts and the mean flow velocity decreases, resulting in the statistical compression of the confined species.

2.2. Irreversible thermodynamics and entropy production in tapered geometries

To analyze the thermodynamics of a single stochastic trajectory Γ(t), the formalism of Seifert is adopted, where total entropy production decomposes into the system entropy change and the medium entropy flux. The stochastic system entropy is defined as the trajectory-dependent Shannon entropy

$$s(t) = -k_B \ln P(\Gamma(t),t) \tag{5}$$

To derive the macroscopic entropy production from this microscopic state, the total trajectory-dependent entropy production rate, defined as the sum of the internal system entropy rate and the medium entropy rate, must be evaluated. First, applying the total time derivative to Eq. (5) via the chain rule yields the internal system entropy rate $\dot{s}(t) = -k_B\frac{\partial_t P(\Gamma,t)}{P(\Gamma,t)} - k_B\dot{\Gamma}.\nabla P(\Gamma,t)$. This partitions the internal rate into the temporal relaxation of the probability distribution and a convective spatial gradient term. Second, for channels with impervious walls, the medium entropy change is strictly thermal, defined by the heat dissipated into the bath $\dot{s_m}(t) = q(t)/T$. Based on the energetics of the overdamped Langevin equation (Eq. 1), this heat dissipation balances the frictional drag against conservative potentials and external driving forces.

The mathematical bridge to deriving the macroscopic field equation occurs when the ensemble average of this total rate $\langle \dot{s_{tot}}(t)\rangle = \langle \dot{s}(t)+\dot{s_m}(t)\rangle$ is performed, by integrating over the entire probability space. To resolve this integral, the temporal relaxation term (∂_t P) is substituted using the Fokker-Planck continuity equation (Eq. 2). Subsequently, by applying integration by parts, and assuming vanishing probability currents at the phase-space boundaries, the complex cross-terms between the stochastic velocity, the external forces, and the diffusive gradients algebraically consolidate. This integration systematically reduces the total ensemble-averaged entropy production rate to a strictly non-negative quadratic form of the probability currents

$$\langle\sigma(t)\rangle = \int d\Gamma\left[\sum_{k=1}^{N}\frac{\gamma_i J_k(\Gamma,t)^2}{TP(\Gamma,t)}\right] \tag{6}$$

where σ represents the entropy production rate and γ is the friction coefficient (drag).

It is important to clarify that the emergence of this quadratic form does not phenomenologically assume or require the probability currents (J_k) to be linear functions of the spatial coordinates. Rather, it is an exact macroscopic consequence of the Fokker-Planck continuity relation and the underlying linear microscopic drag. Because the Fokker-Planck equation enforces probability conservation ($\partial_t P = -\nabla.J$), applying it via integration by parts mathematically cancels out all reversible energetic exchanges with conservative potentials. What continues the integration is the irreversible frictional power dissipated by the probability fluid moving through the thermal bath. In this overdamped regime, the local mean velocity of the probability distribution is defined precisely as $v_k = J_k/P$. Because frictional power inherently scales as the square of the velocity ($\gamma_i v_k^2$), weighting this power by the local probability density P and substituting this mean velocity directly produces the non-negative $\gamma_i J_k^2$ /P term inside the ensemble integral. Thus, the macroscopic entropy production is mathematically bound to a quadratic form driven by the microscopic linear response to thermodynamic forces.

Eq. (6) quantifies the irreversible thermodynamic cost of the mixing process and the uniform frictional resistance along the channel length. In the open semipermeable system, the medium entropy must be redefined to account for matter exchange. When a permeating particle exits the channel, it enters an external reservoir with chemical potential, carrying away both energy and entropic information. The modified rate of medium entropy change thus incorporates this chemical work term

$$s_{perm}(t) = \frac{q(t)}{T} - \frac{\mu_{perm}(z)-\mu_{ext}}{T}n_{out}(t) \tag{7}$$

where q is the dissipated heat rate, μ_{ext} is the specific chemical potential of external reservoir and n_{out} is a stochastic train of delta functions representing discrete leakage events.

Within this overdamped Langevin formalism, the dissipated heat rate is physically generated by the frictional work exerted by the particle as it continuously thermalizes with the macroscopic boundaries. Furthermore, for an ideal Knudsen gas, the local chemical potential is thermodynamically linked to the localized probability density via the relation $\mu_{perm}(z) = \mu_0 + k_B\ T\ \ln(P_{perm}(z))$. These specific trajectory-dependent variables act as the fundamental theoretical intermediaries bridging the discrete microstates to the continuous macroscopic fields. When averaged over the entire particle ensemble, the expected value of the stochastic heat dissipation mathematically transforms into the quadratic bulk frictional dissipation term. Simultaneously, the discrete chemical work driven by the potential difference ($\mu_{perm}(z)$ - μ_{ext}) translates directly into the continuum logarithmic boundary flux. Consequently, the ensemble-averaged local entropy production separates into these two distinct macroscopic regimes

$$\langle\sigma_{tot}\rangle = k_B\int_V dV\left(\frac{J_{conf}^2}{D_{conf}P_{conf}}+\frac{J_{perm}^2}{D_{perm}P_{perm}}\right)+k_B\int_{\delta V}dS.J_{leak}\ln\left(\frac{P_{perm}(z)}{P_{ext}}\right) \tag{8}$$

where the subscript conf means particle species that is trapped inside the channel, leak refers to particles crossing the boundary from inside the channel to the outside, and ext refers to thermodynamic state of the environment outside the channel walls.

For a local probability density $P_{perm}(z)$, this logarithmic boundary term $\Delta\mu = k_BT\ \ln(P_{perm}(z)/P_{ext})$, localizes maximum dissipation at the inlet. In the antidispersion regime, this term dominates the global

budget, and the entropic expansion of the leakage flux effectively compensates for the local ordering of the confined species, thereby satisfying the second law ($\sigma_{tot} \geq 0$).

To analyze the probability of these rare antidispersion trajectories, the fundamental time-reversal symmetry of Langevin dynamics is utilized. This symmetry dictates that the log-ratio of the probability of observing a forward trajectory $P[\Gamma]$ to its time-reversed counterpart $\widetilde{P}[\widetilde{\Gamma}]$ equals the normalized total entropy production, establishing the detailed fluctuation theorem [31,32]

$$\frac{P[\Gamma]}{\widetilde{P}[\widetilde{\Gamma}]} = \exp\left(\frac{\Delta S_{tot}[\Gamma]}{k_B}\right) \tag{9}$$

For the semipermeable open system, the time-reversed conjugate of a leakage event involves a particle spontaneously emerging from the wall against the gradient, an event exponentially suppressed by the chemical potential difference. Thus, the standard path probability is modified using the Crooks fluctuation theorem [33] extended to grand canonical ensembles

$$\frac{P[\Gamma]}{\widetilde{P}[\widetilde{\Gamma}]} = \exp\left[\frac{W - \Delta F - \left(\mu_{perm}(z) - \mu_{ext}\right)\Delta N}{k_B T}\right] \tag{10}$$

where W represents the external mechanical work done on the system during the specific trajectory Γ, ΔF is the equilibrium free energy between the final state and the initial state, and ΔN represents the net change in the number of particles in the channel during the trajectory.

Eq. (10) codifies the trade-off inherent in antidispersion. The probability of spontaneous concentration is exponentially weighted by the chemical work associated with the permeating flux. The validity of the integral fluctuation theorem during this compression implies that, for high-selectivity membranes, the local ordering of the confined species is thermodynamically compensated by heavy non-Gaussian tails in the entropy production distribution.

To evaluate the specific geometric cost of longitudinal transport in a tapered channel, the kinetic theory of diffuse reflection is referenced. The fundamental source of thermodynamic irreversibility is the stochastic interaction with macroscopic boundaries, which effectively randomizes the incident momentum vector. This boundary condition is modeled via the Knudsen cosine law, which assumes perfectly thermalized, rough walls. Because the system operates strictly within the free-molecular regime where intermolecular scattering is absent, thermalization at the wall constitutes the sole mechanism for mechanical dissipation, effectively erasing the directional memory of the particle.

To formalize this mechanism, if this irreversibility is evaluated as the relative entropy between the highly correlated angular distribution that would be preserved under an ideal specular mirror reflection and the fully randomized Knudsen cosine distribution of diffuse reflection, the result evaluates to a positive, constant informational penalty per impact. This acts as an irreducible, discrete quantum of thermodynamic exergy destruction. Because this microscopic relative entropy jump is fixed by the fundamental boundary scattering kernel, the aggregate thermodynamic dissipation is governed entirely by the geometric collision frequency.

While Eq. (8) establishes the localized rate of entropy production in a continuous field, evaluating cascade performance requires translating this local discrete penalty into a global geometric cost. Thus, Eq. (11) is not a direct algebraic derivation of Eq. (8), but rather its macroscopic spatial integration. By integrating this constant discrete relative entropy penalty against the spatial collision rate (which scales proportionally with the local longitudinal flux and inversely with the local transverse dimension) over the entire tapering longitudinal domain, the global geometric entropy generation is derived. In this macroscopic formulation (Eq. 11), the absolute magnitude of informational penalty per impact is mathematically absorbed into the overarching system aggregation constant, ensuring the geometric optimization framework remains scale-invariant. While the preceding fluctuation theorems establish the fundamental existence and bounds of the localized entropic costs, integrating these exact, trajectory-dependent probabilities across the entire domain remains analytically intractable for cascade design. Therefore, evaluating overarching geometric performance requires a transition from these exact stochastic bounds to a mean-field approximation.

For a channel tapering linearly from W_{in} to W_{out}, defined by a tapering ratio $\chi = W_{out}/W_{in}$ and a dimensional reduction gradient $\alpha = (1-\chi)/L$, the transverse dimension is $W(z) = W_{in}(1-\alpha z)$. Integrating this cost over a linear χ and combining it with the exponential depletion of flux $J(z)=J_0 \exp(-z/\lambda)$, the global macroscopic entropy generation integrates to

$$S_{gen} = \frac{\kappa}{\alpha}\exp\left(-\frac{1}{\alpha\lambda}\right)\int_{\chi}^{l}\frac{1}{u}\exp\left(\frac{u}{\alpha\lambda}\right)du \tag{11}$$

where S_{gen} represents the total entropy generation, u represents the normalized channel width at a specific point z, and κ aggregates the system constants.

From a structural standpoint, it is important to distinguish the theoretical nature of this formulation from the preceding mathematics. While Eqs. (5) through (10) represent exact, fundamental thermodynamic relations stated by stochastic fluctuation theorems, Eq. (11) constitutes an applied, macroscopic geometric approximation. By mathematically abstracting the physical collision rate as continuously inversely proportional to the local channel width, this approximate formulation serves as the necessary analytical bridge connecting fundamental stochastic kinetic theory to the practical structural optimization of the cascade.

Eq. (11) is a direct manifestation of the generalized exponential integral function. Notice that in the uniform pipe limit ($\chi \to 1$), the integral simplifies, and the total entropy generation scales linearly with penetration distance, entirely governed by the natural decay length λ. Conversely, in the severe taper limit where the exit is severely choked ($\chi \to 0$), the singularity at the origin causes the integral to diverge logarithmically ($S_{gen} \to \infty$). This demonstrates that forcing a finite flux through an infinitesimally narrow exit necessitates an infinite number of diffuse collisions, mathematically destroying separation efficiency.

2.3. Macroscopic efficiency metrics and geometric optimization

To bridge the gap between microscopic stochastic dynamics and the optimization of multi-stage separation cascades, the objective functions governing macroscopic thermodynamic efficiency are formalized. The primary utility of the separation process is quantified by the separation work gain defined as the reduction in the Gibbs-Shannon mixing entropy between the feed and the bifurcated product streams

$$W_{sep} = S_{mix,it} - \left(S_{mix,perm} + S_{mix,ret}\right) \tag{12}$$

where W_{sep} is the separation work gain, $S_{mix,it}$ is the mixing entropy of the system in its initial state before separation occurs, $S_{mix,perm}$ is the mixing entropy of the specific population of particles that successfully passed through the membrane, and $S_{mix,ret}$ is the mixing entropy of the specific population of particles that were retained by the membrane.

It is important to formally classify the thermodynamic nature of these quantities. While the internal ballistic transport through the cascade is a highly non-equilibrium process driven by stochastic entropy production, the evaluation of W_{sep} relies on the local equilibrium hypothesis at the system boundaries. Because the upstream feed and external permeate environments operate as ideal, infinite reservoirs, their thermodynamic states are rigorously defined by classical equilibrium state variables. Consequently, by balancing the ideal, reversible minimum work required to un-mix the streams (W_{sep}) against the irreversible continuous exergy destruction of the internal flow (S_{gen}), the

subsequently defined efficiency metric functions fundamentally as a second law (exergetic) efficiency, rather than a first law energy balance.

Within the context of isothermal stochastic thermodynamics, this macroscopic separation work represents the useful energy conversion of the system. Specifically, it quantifies the available free energy successfully utilized to un-mix the binary gas stream, driven by the localized chemical potential gradients across the selectively permeable boundary. However, maximizing this operational energy conversion inherently dictates a structural design compromise. The fundamental trade-off between cascade design and fluid operation lies in the fact that achieving high separation yields in low-affinity systems structurally requires tight geometric confinement (tapering) to mechanically force particle-boundary interactions.

Notice that the thermodynamic cost associated with this separation comes from two distinct sources. Microscopically, momentum erasure via diffuse boundary collisions generates an entropic penalty (e.g., scaling as $n_{coll}+\delta_p$, where n_{coll} accounts for particle collisions and δ_p for the permeation event). Macroscopically, geometric constriction in tapered channels induces significant backscattering, quantified by the forward throughput ratio Φ_{fwd}.

A simple maximization of the ratio W_{sep}/S_{gen} is theoretically insufficient for open systems, as it artificially diverges toward a zero-flux dead-end configuration by entirely neglecting macroscopic transport penalties. To establish a rigorous basis for optimization, an objective function is constructed that balances the thermodynamic utility (W_{sep}) against two simultaneous, yet distinct, evolutionary costs: the intrinsic microscopic dissipation (S_{gen}) and the induced macroscopic transport penalty ($1-\Phi_{fwd}$). To isolate the influence of geometry from intrinsic material properties, the specific separation thermodynamic efficiency is introduced, which normalizes this overall balance against the baseline transmission probability of the selected membrane. Rather than a derived fundamental thermodynamic limit, this metric is formulated as a phenomenological objective function. It is constructed to dynamically weigh the idealized thermodynamic utility against two competing, yet dimensionally normalized, modes of systemic failure

$$\eta_{ST} = \frac{W_{sep}}{P_{trans}\left[S_{gen} + \left(1 - \Phi_{fwd}\right)\right]} \tag{13}$$

where η_{ST} is the specific separation thermodynamic efficiency, P_{trans} is the intrinsic surface affinity or permeability of the selective boundary material and represents the probability that a particle hitting the wall will permeate rather than reflect, and Φ_{fwd} is he ratio of incident flux that successfully traverses the active control volume longitudinally and quantifies the macroscopic transport efficiency, distinguishing particles that flow through the channel from those that backscatter out the inlet.

Regarding the mathematical properties of Eq. (13), η_{ST} evaluates as a dimensionless, phenomenological objective function. The thermodynamic terms (W_{sep} and S_{gen}) are computationally normalized against the thermal energy ($k_BT = 1$), effectively rendering them as dimensionless informational quantities. Consequently, the denominator represents an unweighted scalarization of two distinct, dimensionless system penalties: the cumulative microscopic informational loss (S_{gen}) and the macroscopic kinematic rejection probability ($1-\Phi_{fwd}$). By assigning an implicit equal weight (a 1:1 scalarization) to these variables, the framework establishes a compound penalty index. It is important to note that, within this highly restricted Knudsen flow regime, the forward throughput ratio ($\Phi_{fwd}<<1$) renders the kinematic rejection penalty essentially static. Because its gradient across the morphological spectrum is mathematically negligible compared to the variance in localized frictional entropy (S_{gen}), this term acts as an irreducible, near-constant baseline cost of geometric confinement. Therefore, the specific choice of scalarization weight shifts only the absolute magnitude of the objective function, preserving the critical inflection points and the location of the structural optimum. Furthermore, the bounds of this specific efficiency are strictly non-negative, evaluating within the domain $\eta_{ST} \in [0, \eta_{max}]$. The lower bound of zero corresponds to a complete failure to separate the binary mixture ($W_{sep} = 0$). While bounded above by a finite maximum (η_{max}), it does not strictly asymptote to unity like a classical Carnot cycle efficiency. This is because the free-molecular flow physically requires a positive number of momentum-erasing wall collisions to traverse the longitudinal domain ($S_{gen} > 0$), meaning the denominator can never vanish. This ensures the metric operates as a mathematically stable, finite objective function for evaluating morphological viability.

In formalizing this thermodynamic optimization, the global driving forces of the system (specifically the chemical potential gradients bounding the control volume) are strictly constrained as fixed boundary conditions. Therefore, sweeping the geometric tapering parameter does not artificially alter the available thermodynamic forces. Instead, it dynamically modulates the internal mechanical resistance of the active control volume. Finding the optimal tapering ratio does not conflict with the principles of maximum efficiency versus maximum dissipation. Rather, the peak of η_{ST} precisely identifies the structural inflection point where the exergetic gains achieved by mechanically forcing localized permeation are perfectly overtaken by the exponentially rising thermodynamic costs of geometrically induced momentum erasure and backscattering.

Eq. (13) decouples geometric performance from membrane chemistry. Maximizing η_{ST} reveals a critical morphological transition. This critical morphological transition is defined as the fundamental shift in optimal channel architecture dictated by the overarching thermodynamic limits of the boundary. Specifically, it represents the structural divergence where low-affinity membranes require severe tapering to force collisions and increase the frequency of membrane interactions, whereas high-affinity membranes favor uniform geometries to mitigate parasitic transport penalties.

It is also important to note that while η_{ST} serves as a theoretical objective function for computational cascade design, it is not a directly accessible empirical observable. In a physical laboratory setting, the discrete microscopic entropic penalties cannot be mechanically isolated by standard instrumentation. Instead, experimental validation of this geometric optimization framework requires measuring the macroscopic phenomenological analogues of these theoretical terms. Specifically, an experimentalist must proxy this efficiency by evaluating the empirical stage cut and species separation factor to derive the macroscopic W_{sep}, tracking the steady-state retentate mass flow rates to infer Φ_{fwd}, and measuring the required isothermal compressor work (specifically the pressure drop necessary to sustain the Knudsen flow) as the bulk macroscopic manifestation of the microscopic thermodynamic dissipation.

3. Computational methodology

To investigate the non-equilibrium transport dynamics of a binary gas mixture traversing a tapering cascade within the Knudsen regime, a Test Particle Monte Carlo (TPMC) solver was developed. This numerical approach is designed to resolve the mathematical formalism established in Section 2. Specifically, the TPMC solver acts as the computational engine for the Langevin equation (Eq. 1), mapping the theoretical continuous stochastic process into discrete ballistic flights interrupted by wall collisions. Because intermolecular scattering is absent in the Knudsen regime, the theoretical frictional damping (γ_i) and thermal fluctuations ($\xi_k(t)$) defined in our analytical model are strictly imparted through the Knudsen cosine scattering at the boundaries. By tracking a massive ensemble of these individual Markovian trajectories, the solver statistically reconstructs the macroscopic probability densities and permeation fluxes governed by the Fokker-Planck formulation (Eq. 4). Computational architecture employs a Lagrangian particle-tracking algorithm specifically optimized for ballistic transport, facilitating high-throughput geometric optimization. By decoupling convective spatial displacement from stochastic boundary interactions, this formalism

provides a physical solution to the Boltzmann transport equation in the strict Knudsen limit, wherein the molecular mean free path vastly exceeds the characteristic transverse dimension of the channel.

To facilitate a scale-invariant analysis, the simulation employs a system of reduced dimensionless units. The particle mass is normalized to m= 1 and the thermal energy to $k_BT = 1$. Consequently, the mean thermal velocity is set to $\bar{v}_{th} = \sqrt{8/\pi}$, and the characteristic length scale is normalized to the inlet width $W_{in} = 2$. This normalization streamlines the statistical analysis of entropy variance and ensures that the computed efficiency metrics are independent of specific molecular weights or absolute temperatures.

The system phase-space evolution is tracked within a two-dimensional, planar control volume bounded by a continuous converging manifold (Fig. 1). The spatial domain is aligned along the longitudinal coordinate $z \in [0,L]$ and symmetrically confined in the transverse direction. Although the spatial boundaries are confined to a two-dimensional geometric plane, the simulation rigorously tracks three-dimensional velocity vectors for all particles to preserve the correct thermal kinetic energy distribution during boundary scattering. To execute the simulation, this spatial domain is governed by three defined mathematical boundary conditions. The inlet at $z = 0$ operates as a thermodynamic source, injecting particles sampled from a constant-temperature semi-Maxwellian distribution. The terminal exit at $z = L$ acts as a perfect vacuum sink, where particles are permanently absorbed, truncated from the active domain, and tallied for macroscopic throughput. Finally, the lateral walls are defined by the analytical algebraic inequalities $y \leq \pm\ 0.5\, W(z)$, functioning as reactive or reflective manifolds depending on the species. The channel topology is defined through analytic algebraic inequalities, precluding the necessity for body-fitted spatial meshing. The fundamental dimensions are set to an entrance width of W_{in}= 2 and a longitudinal extent of L= 50. This pronounced 25:1 aspect ratio was critically selected to guarantee the emergence of a fully developed Knudsen flow profile, effectively suppressing transient entrance effects.

The transverse dimension follows a linear tapering profile defined by $W(z) = W_{in}\,(1-\alpha\, z)$ where, as mentioned, the reduction gradient is given by $\alpha = (1- \chi)/L$. To evaluate the morphodynamics of localized permeation hotspots, the control volume is simulated across a parametric sweep of constriction ratios $\chi \in [\ 0.10, 1.00]$.

Because the Knudsen assumption implies a zero-potential landscape within the channel bulk, particle motion is strictly inertial. The discrete time evolution of the system over a maximum integration step $\Delta t = 10^{-3}$ initiates with a free-flight propagation phase. Because inter-collision forces are zero, the position update relies on an exact analytical ballistic propagation, $r(t + \Delta t)=r(t) + v(t)\Delta t$, rather than a numerical approximation. Following each proposed update, the algorithm performs strict collision detection by evaluating the trajectory ray against the lateral boundary inequalities. If an intersection is detected during the Δt interval, the exact sub-step collision coordinate is calculated geometrically. The particle is halted precisely at this boundary intersection to enforce volume exclusion, its momentum vector is randomized according to the local wall normal, and the remaining fractional time step is expended propagating the particle away from the wall along its newly assigned trajectory. To drive the stochastic sampling required for inlet thermalization and diffuse scattering, a Mersenne Twister pseudo-random number generator [34] is employed, ensuring statistical independence and minimizing correlation artifacts in the resultant entropy production maps.

To obtain statistical robustness and resolve the local entropy production variance, the simulation tracks a massive aggregate ensemble of $N = 2 \times 10^5$ test particles. To verify statistical convergence, this total population is partitioned into independent computational batches. By evaluating the variance of the macroscopic observables across these sequential batches, it is ensured that the standard error of the mean asymptotes to a negligible fraction of the bulk value, confirming that the Monte Carlo integration has achieved statistical steady-state and adequately sampled the available phase space.

The TPMC solver was developed as a custom, in-house continuous-space tracking script. This ensemble is strictly initialized at the inlet plane ($z = 0$) by sampling injection velocities from a forward-directed, semi-Maxwellian flux distribution, accurately mimicking particle effusion from a constant-temperature, constant-pressure upstream reservoir into the Knudsen domain.

The binary mixture is modeled by partitioning this ensemble into two distinct populations. The inert species A ($N_A = 10^5$) is subject to strictly reflective boundary conditions, where particle-wall collisions undergo diffuse reflection governed by the Knudsen cosine law. The post-collision velocity vector is effectively randomized according to the local wall normal, thermalizing the particle with the boundary. Algorithmic implementation of this thermalization is achieved via explicit inverse transform sampling. For each diffuse reflection, the post-collision azimuthal angle ϕ is sampled uniformly from the interval $[0, 2\pi]$, while the polar angle θ (measured relative to the local wall normal) is sampled from a probability density function proportional to $\cos(\theta)\sin(\theta)$. To prevent mesh discretization errors, the local wall normal vector is analytically updated at every collision event as a strict trigonometric function of the local dimensional reduction gradient α, ensuring the backward-facing solid angle of the taper is perfectly resolved during particle trajectory updates.

Computationally, this stochastic randomization process acts as the precise physical mechanism for the momentum erasure and discrete entropy production discussed in Section 2.2, thereby directly linking the local geometric collision rate to the global thermodynamic dissipation. The permeable species B ($N_B = 10^5$) is governed by a stochastic Monte Carlo rejection scheme upon every wall impact. While this population partition establishes a 1:1 equimolar baseline for the simulation, it is critical to note that the strict free-molecular nature of the flow guarantees that intermolecular scattering is entirely suppressed, rendering all stochastic trajectories physically non-interacting. Therefore, altering the relative proportion of inert to permeable particles in the initial feed does not alter the underlying kinematic dynamics, spatial collision frequencies, or the species-specific exponential depletion profiles. Although the absolute magnitude of the macroscopic separation work inherently scales with varying initial feed compositions, the

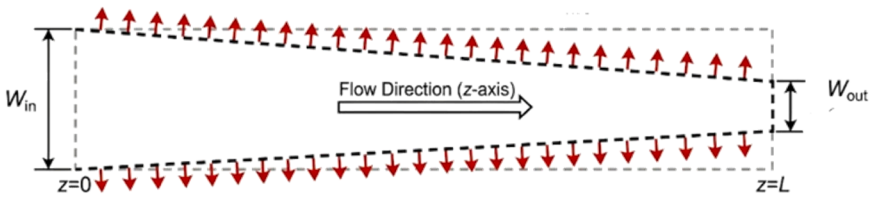

Fig. 1. Schematic representation of the tapering cascade geometry modeled as a two-dimensional continuous control volume. The spatial domain is aligned along the primary flow axis (z-axis), with the channel width monotonically tapering from an initial entrance dimension W_{in} at $z = 0$ to a terminal exit dimension W_{out} at $z = L$. The dashed upper and lower boundaries represent the selectively permeable macroscopic walls. The outward-pointing red arrows illustrate the local, spatially resolved permeation flux of the active species (species B), which is stochastically extracted from the domain upon collision. The inert species (species A) experiences these same boundaries as perfectly impervious, undergoing strictly diffuse reflection to sustain the continuous forward flow.

independent mechanical transport of each individual species remains perfectly invariant. This mechanism is driven by the intrinsic transmission probability P_{trans} evaluated at distinct regimes (0.015, 0.030, 0.045). It is important to contextualize the magnitude of these parameters. While a transmission probability of 1.5–4.5% may appear numerically modest, these values are highly representative of the per-collision mechanics governing state-of-the-art, high-selectivity molecular sieves (such as zeolites or carbon molecular sieves). In such physical systems, pore entry is regulated by severe steric hindrance and activation energy barriers, meaning the vast majority of instantaneous wall impacts result in diffuse reflection rather than successful permeation. However, this small discrete probability does not yield a minor macroscopic effect. Because the high-aspect-ratio Knudsen channel ($L/W_{in} = 25$) inherently forces hundreds to thousands of boundary interactions per particle trajectory, this modest per-collision probability compounds exponentially, driving the massive macroscopic flux depletion observed in the steady-state reaction-diffusion profiles.

For each collision event k, a random variable $\xi \in [0, 1]$ is generated to determine the trajectory. If $\xi < P_{trans}$, the particle permeates and is permanently truncated from the active domain, whereas if the condition fails, it undergoes standard diffuse reflection.

To reconstruct the macroscopic observables from microscopic trajectories, the longitudinal domain is discretized into M= 100 equidistant spatial bins. The spatially resolved longitudinal permeation flux is computed by histogramming the coordinates of all successful leakage events. This discrete distribution is normalized by the local surface area element and the total simulation time to yield the probability density function of permeation

$$J_{wall}(z_j) = \frac{1}{\Delta t\, \Delta A_j} \sum_{i=1}^{N_{leak}} \delta(z_i \in bin_j) \tag{14}$$

Eq. (14) is essential for identifying the entropy expansion zones where the boundary term dominates the dissipation budget.

To compute the specific separation thermodynamic efficiency, the solver tracks the complete interaction history of every particle, enabling an ensemble average of the microscopic behavior. The S_{gen} is quantified by maintaining a cumulative counter for each trajectory that aggregates the discrete entropic penalty of every wall reflection and stochastic permeation event, strictly adhering to the formulation in Eq. 11. The continuous spatial integration detailed in the theoretical framework is resolved via a discrete Monte Carlo summation. For every verified boundary collision occurring at a specific longitudinal coordinate z_c, the specific trajectory's entropy counter is incremented by a discrete penalty proportional to the localized geometric constriction, scaling as $1/W(z_c)$. By averaging these discrete cumulative sums over the entire N-particle ensemble, the solver statistically converges upon the global macroscopic entropy generation. This microscopic cost is balanced against the macroscopic throughput Φ_{fwd} which is evaluated by determining the fraction of the incident ensemble that successfully traverses the exit plane at $z = L$. Because the forward throughput ratio fundamentally represents a discrete success-or-failure probability for independent, non-interacting particle trajectories, its statistical uncertainty is governed by the binomial standard error, expressed as $\sigma_\Phi = \sqrt{\frac{\Phi_{fwd}(1-\Phi_{fwd})}{N}}$. Similarly, the statistical uncertainty of the continuous global entropy generation is bound by the variance of the trajectory ensemble. Because the simulation tracks a massive aggregate ensemble ($N = 2 \times 10^5$), the Monte Carlo sampling noise is heavily suppressed. For the forward throughput ratio, applying the binomial standard error to the empirical maximum throughput ($\Phi_{fwd,max} \approx 0.018$) yields a strictly bounded maximum statistical uncertainty of approximately $\sigma_\Phi < 3 \times 10^{-4}$. Because this resulting statistical variance is extremely small (orders of magnitude lower than the macroscopic parametric shifts observed across the morphological spectrum) the statistical robustness of the calculated performance metrics is mathematically guaranteed.

The separation work is derived by evaluating the final mixing entropies from the evolved concentration fractions of species A and B within the bifurcated permeate and retentate populations. The integration of these diagnostics facilitates the mapping of η_{ST} across the morphological parameter space (χ, P_{trans}), thereby establishing a direct link between the statistical mechanics of single-particle trajectories and the macroscopic optimization of the cascade architecture.

4. Results and discussion

To elucidate the fundamental transport dynamics governing the gas mixture within the tapering cascade, the purely geometric contribution to flow resistance is first isolated by examining the system under strictly impervious boundary conditions. Fig. 2 presents the simulated ballistic trajectories generated by the Lagrangian particle-tracking algorithm for a non-permeating species. The figure illustrates the spatial distribution of stochastic Knudsen trajectories across varying constriction ratios, within the high-aspect-ratio conduit. In the strongly tapered regime (χ=0.25), a pronounced geometric rectification effect emerges. The steep inclination of the converging boundary walls presents a substantial backward-facing solid angle to incident particles. Consequently, a high concentration of backscattered trajectories becomes trapped near the channel entrance. This severe geometric constriction induces significant macroscopic backscattering, which fundamentally impairs longitudinal transport and degrades the forward throughput ratio of the system. As the geometric confinement is relaxed toward a weakly tapered configuration (χ=0.75), the reduction in the transverse dimensional gradient fundamentally alters the effective collision landscape. The diminished backward-facing solid angle facilitates much more efficient forward propagation along the longitudinal coordinate, mitigating the parasitic transport penalties associated with inlet backscattering.

This baseline, zero-permeability behavior highlights the intrinsic thermodynamic irreversibility associated with momentum erasure during diffuse boundary collisions. Each wall interaction constitutes a discrete entropy production event. So, severe tapering mechanically forces an increased spatial collision rate, establishing a severe geometric and thermodynamic cost for macroscopic transport prior to the introduction of any selective membrane permeability.

The open semipermeable system is now considered, where the symmetry between the two gas species is fundamentally broken. Fig. 3 delineates the morphological evolution of this binary Knudsen transport, juxtaposing the purely reflective trajectories of the inert species A (blue traces) against the stochastic absorption of the selectively permeable species B (orange traces). The explicit mapping of discrete permeation loci (red markers) along the lateral boundaries provides direct visual confirmation of the theoretically predicted macroscopic behavior, the transformation of the steady-state density into a reaction-diffusion profile that exhibits an exponential decay. This spatial distribution physically signifies that the vast majority of the permeating species is extracted near the channel inlet. As these permeating particles systematically escape the control volume, the effective collision landscape shifts and the mean flow velocity decreases, which subsequently results in the statistical compression of the confined inert species further down the longitudinal domain.

The top row of the Fig. 3 matrix illustrates the non-equilibrium dynamics for a low-affinity membrane (P_{trans}=0.015). In the weakly tapered configuration (χ=0.90), the reduced wall curvature diminishes the spatial collision rate, leading to an insufficient interaction frequency and sparsely distributed permeation events. To overcome this low intrinsic permeability, the system requires severe tapering (as seen in the χ=0.25 and χ=0.50 configurations) to mechanically force boundary collisions and artificially inflate the total number of membrane interactions per particle. This forced interaction imposes a severe thermodynamic penalty. While the structural constriction successfully enhances the overall separation work gain by driving permeation, it simultaneously inflates the entropy generation through repeated

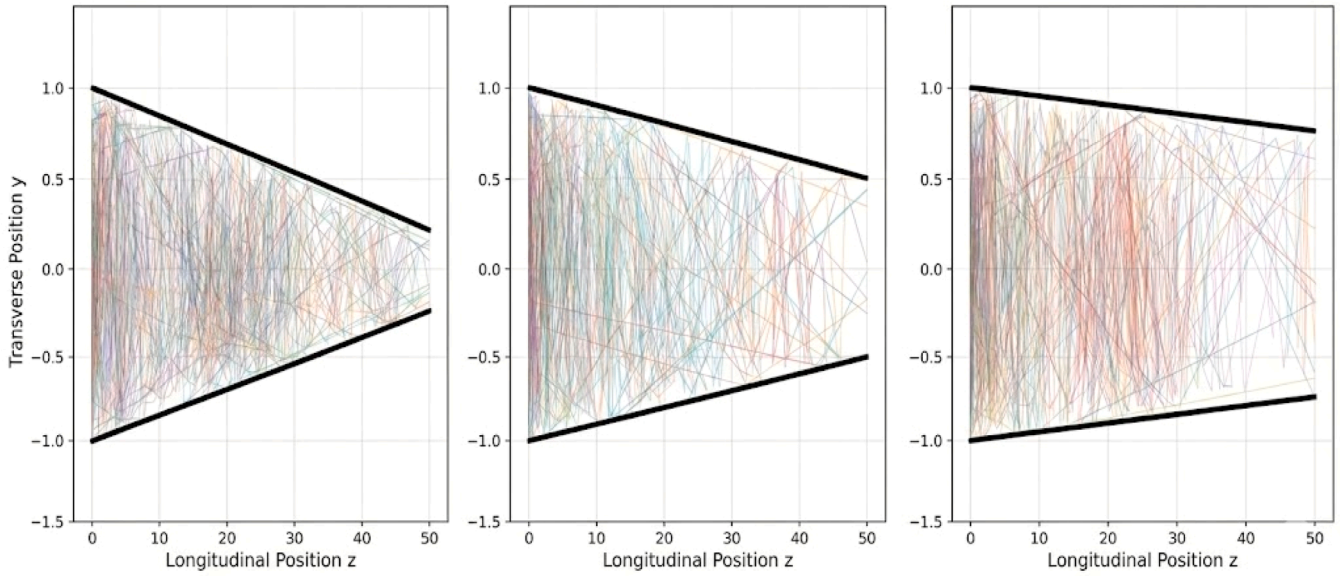

Fig. 2. Knudsen particle scattering profiles across varying tapering ratios with impervious boundaries. The panels illustrate simulated ballistic trajectories for constriction ratios of 0.25 (left), 0.50 (center), and 0.75 (right), isolating the purely geometric contribution to flow resistance (P_{trans}=0). In the strongly tapered regime (χ=0.25), a pronounced geometric rectification effect is observed, characterized by a high concentration of backscattered trajectories trapped near the channel entrance due to the steep wall inclination opposing the forward flow direction. As the geometric confinement is relaxed toward the weakly tapered configuration (χ=0.75), the reduction in wall curvature diminishes the backward-facing solid angle presented to colliding particles.

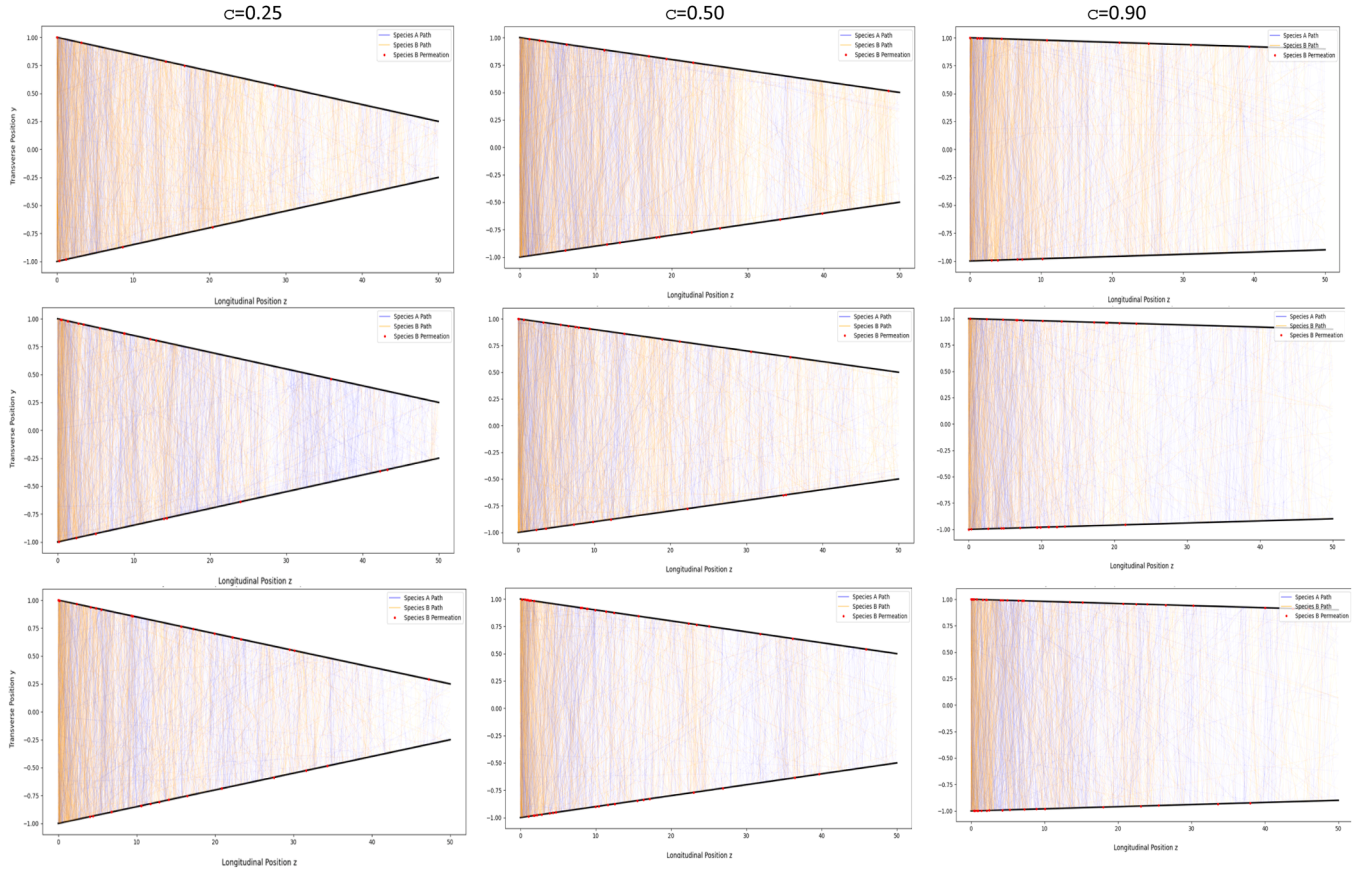

Fig. 3. Morphological evolution of binary Knudsen transport and permeation hotspots across varying geometric confinements and surface affinities. The matrix visualizes the stochastic trajectories of an equimolar gas mixture traversing a longitudinal domain of L= 50, comprising an inert Species A (blue traces, P_{trans}=0) and a selectively permeable Species B (orange traces). Red loci along the lateral boundaries represent discrete, successfully resolved permeation events. The columns contrast strongly tapered (χ=0.25), moderately tapered (χ=0.50), and weakly tapered (χ=0.90) channel geometries, while the rows evaluate low (P_{trans}=0.015), intermediate (P_{trans}=0.030), and high (P_{trans}=0.045) intrinsic membrane permeabilities.

momentum erasure via diffuse boundary collisions and penalizes macroscopic transport by inducing significant backscattering. So, the intermediate geometry optimally balances the necessary collision forcing against these parasitic transport penalties, aligning with the previously established maximization of the specific separation thermodynamic efficiency.

The bottom row of Fig. 3 captures the transport paradigm for high-affinity membranes (P_{trans}=0.045). In this regime, the intrinsic surface transmission probability is sufficiently elevated that species B particles readily permeate upon wall impact, precluding the need for geometrically induced collision forcing. The exponential depletion of the permeating flux is highly pronounced, and the logarithmic boundary term heavily dominates the global dissipation budget, localizing the maximum thermodynamic dissipation squarely at the inlet. Because the separation mechanism is inherently efficient at the boundary level, imposing severe geometric constrictions (χ=0.25) yields no separation benefit and merely induces unrecoverable parasitic transport penalties that degrade the forward throughput ratio. This visual matrix confirms the critical morphological transition dictated by the overarching theoretical framework. While low-affinity membranes rely on severe geometric tapering to function, high-affinity selective boundaries fundamentally favor more uniform geometries to maximize overall thermodynamic efficiency.

To quantify the macroscopic observables derived from the microscopic trajectories, Fig. 4 presents the spatially resolved longitudinal permeation flux, evaluated across the associated parametric space of tapering ratios and intrinsic membrane permeabilities. This spatially resolved longitudinal permeation flux is computed by histogramming the coordinates of all successful leakage events for the active species. The resulting histograms directly confirm the theoretical framework assertion that the system transforms the steady-state density into a reaction-diffusion profile exhibiting exponential decay. The dashed exponential fit lines visually reinforce this behavior, physically demonstrating that the majority of the permeating species is extracted near the inlet. An analysis of the histogram matrix reveals the highly coupled influence of surface affinity and geometric confinement on the characteristic decay length. As the intrinsic transmission probability increases from the top row (P_{trans}=0.015) to the bottom row (P_{trans}=0.045), the decay length shortens. In high-affinity systems, the permeable species is rapidly depleted immediately upon entering the control volume, yielding a steep drop in the localized flux. On the other hand, in the low-affinity regime, the active separation zone extends much deeper into the longitudinal domain. Within this lower permeability tier, a weakly tapered conduit (χ=0.90) allows a significant fraction of particles to traverse the entire longitudinal domain without sufficient boundary interactions to trigger permeation. Imposing a severe geometric constriction (χ=0.25) mechanically amplifies the distal spatial collision rate, forcefully converting these potential escaped trajectories into localized permeation events in the deeper, highly restricted regions of the channel.

The pronounced concentration of permeation events at the channel entrance carries critical macroscopic thermodynamic consequences. Because permeating particles carry away both energy and entropic information, this extraction introduces a logarithmic boundary term governed by the chemical potential difference, which localizes maximum dissipation at the inlet. The spatially resolved flux models in

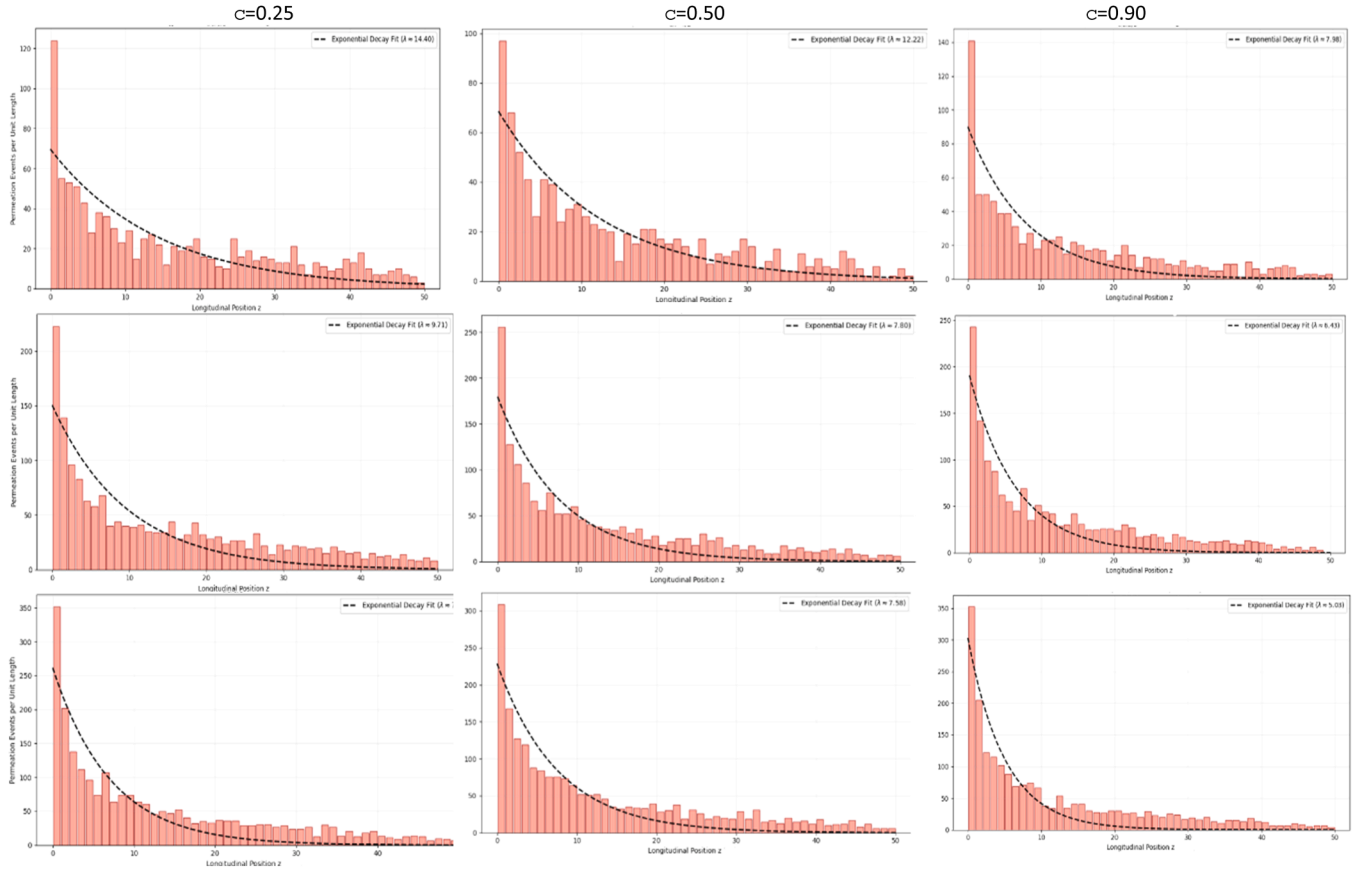

Fig. 4. Spatially resolved longitudinal permeation flux, $J_{wall}(z)$, evaluated across varying tapering ratios and intrinsic membrane permeabilities. The histograms quantify the spatial distribution of discrete permeation events for the active species B along the primary flow axis. The matrix columns represent strongly tapered (χ = 0.25), moderately tapered (χ = 0.50), and nearly uniform cylindrical (χ = 0.90) channel geometries, while the rows correspond to low (P_{trans} = 0.015), intermediate (P_{trans} = 0.030), and high (P_{trans} = 0.045) surface affinities. The dashed black lines denote exponential decay fits following the relation J(z) = a exp(-z/λ), where the characteristic decay length λ defines the longitudinal extent of the active separation zone.

Fig. 4 are essential for identifying the entropy expansion zones where the boundary term dominates the dissipation budget. In summary, whether driven inherently by high membrane permeability or artificially forced via severe geometric tapering, the rapid inlet extraction establishes a severe, highly localized thermodynamic cost that satisfies the second law while enabling the separation of the binary mixture. While the strictly free-molecular nature of this theoretical Langevin framework precludes direct, perfectly matched experimental replication, these spatial extraction profiles exhibit strong qualitative agreement with established macroscopic phenomenological models of continuous membrane cascades. Standard continuum-based permeation models similarly predict sharp exponential decays in local retentate flow near cascade inlets for highly selective barriers. This stochastic methodology inherently recovers this macroscopic limit from first principles, while providing the added resolution of explicit, path-dependent thermodynamic dissipation mapping that bulk continuum models cannot resolve.

The mechanical cost of geometric confinement is depicted in Fig. 5, which illustrates the forward throughput ratio as a function of the tapering profile. As anticipated from the high degree of inlet backscattering inherent to strongly tapered Knudsen conduits, Φ_{fwd} exhibits a stark, monotonic decline as the geometric exit becomes progressively choked ($\chi \rightarrow 0.1$), providing direct proof that severe constriction mechanically impairs longitudinal transport. Furthermore, Φ_{fwd} visibly decreases as intrinsic surface affinity P_{trans} increases. This behavior reflects the rapid depletion of species B flux depicted in Figs. 3 and 4, confirming that efficient side-wall permeation directly reduces the fraction of particles available to reach the distal exit boundary.

Having established the localized thermodynamic costs driven by rapid inlet extraction, the global macroscopic performance of the separation cascade is now evaluated. Fig. 6 illustrates the competing effects of channel constriction on the specific separation thermodynamic efficiency and the total entropy generation for a system bounded by a low-affinity membrane (P_{trans}=0.015). It should be noted that because these two observables operate on vastly different numerical magnitudes, they are plotted on independent primary and secondary vertical axes. Consequently, any visual intersection points between the efficiency and entropy curves across Figs. 6–8 are due to the dual-axis scaling, and the geometric crossing points hold no fundamental mechanical or physical significance.

These results depicted at Fig. 6 reveal a monotonic increase in global macroscopic entropy generation as the channel exit becomes progressively choked ($\chi \rightarrow 0.1$). This reflects the heavy thermodynamic penalty incurred by momentum erasure. As the geometry severely constricts, the spatial collision rate rises very much, forcing an accumulation of diffuse

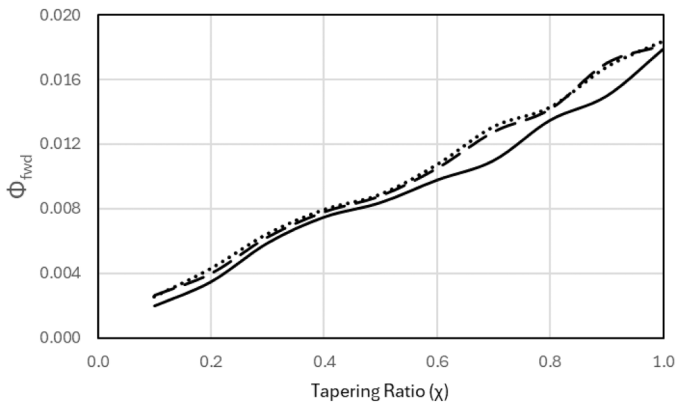

Fig. 5. Evolution of the forward throughput ratio versus tapering ratio across varying surface affinities. The plot illustrates the fraction of incident particles that successfully traverse the complete longitudinal extent of the high-aspect-ratio conduit and reach the exit reservoir, as a function of geometric confinement. Data are presented for low (0.015, dotted curve), intermediate (0.030, dashed curve), and high (0.045, solid curve) intrinsic membrane permeabilities.

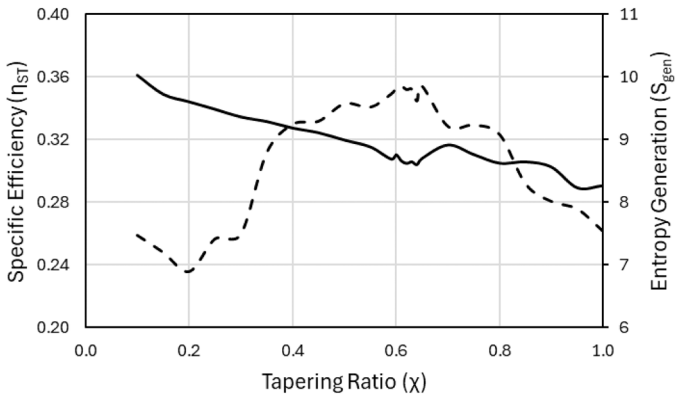

Fig. 6. Morphological dependence of macroscopic thermodynamic efficiency and entropic cost in a stochastic Knudsen flow regime. The plot illustrates the competing effects of channel constriction on the specific separation thermodynamic efficiency (dashed line, left axis) and the total entropy generation (solid line, right axis) as a function of the tapering ratio. Data is presented for a system with a low-affinity selective boundary, characterized by an intrinsic transmission probability of P_{trans}= 0.015.

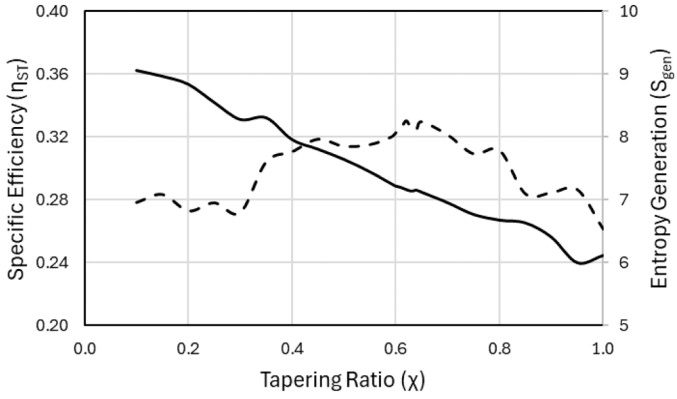

Fig. 7. Morphological dependence of macroscopic thermodynamic efficiency and entropic cost for an intermediate-affinity membrane (P_{trans}= 0.030). The plot shows the evolution of specific separation thermodynamic efficiency (dashed line, left axis) and total entropy generation (solid line, right axis) across a parametric sweep of constriction ratios.

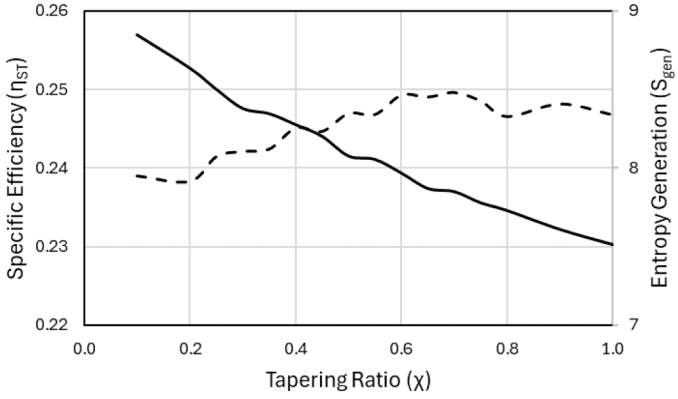

Fig. 8. Morphological dependence of macroscopic thermodynamic efficiency and entropic cost for a high-affinity membrane (P_{trans} = 0.045). The plot displays the specific separation thermodynamic efficiency (dashed line, left axis) and total entropy generation (solid line, right axis) as a function of the tapering ratio.

boundary collisions that irreversibly dissipate energy and increase the overall geometric cost of longitudinal transport.

In contrast to the monotonic rise in entropy generation, the specific thermodynamic efficiency exhibits a distinctly non-monotonic profile across the tapering spectrum. The emergence of a peak optimal intermediate tapering ratio, observed near $\chi \sim 0.65$, signifies a critical morphological balance for low-affinity systems. In this regime, the intrinsic surface permeability is too low to facilitate efficient separation within a uniform cylindrical channel. Therefore, a moderate geometric constriction is fundamentally required to mechanically force wall collisions and maximize the integrated probability of permeation for the mixed species. This intermediate geometry successfully optimizes the trade-off, maximizing the separation work gain while strategically mitigating the severe parasitic macroscopic transport penalties (e.g., excessive inlet backscattering) and the compounding irreversible entropic costs that dominate in highly restricted geometries.

Fig. 7 delineates the system performance for a membrane characterized by an intrinsic transmission probability of $P_{trans}= 0.030$. A comparative examination of the global macroscopic entropy generation reveals a visible overall reduction relative to the low-affinity system, with the total entropic cost now constrained to visibly lower absolute limits. This thermodynamic relief is related directly from the increased boundary permeability. As particles undergo stochastic absorption more readily upon wall impact, they exit the longitudinal domain and enter the external reservoir before accumulating an extensive history of diffuse reflections. So, the system naturally bypasses the compounding discrete entropic penalties that are typically generated by the continuous randomization of the incident momentum vector during prolonged, geometrically trapped wall collisions. Simultaneously, the specific separation thermodynamic efficiency profile begins to exhibit the onset of a critical morphological transition. While the η_{ST} curve maintains a non-monotonic shape with an optimal performance peak remaining near $\chi \sim 0.60$–0.65, this optimal zone distinctly broadens into a wider plateau. This subtle but crucial structural shift illustrates that as the intrinsic surface affinity increases, the fundamental necessity to mechanically force collisions via steep dimensional reduction gradients inherently diminishes. Because the active species permeates more efficiently on its own, the system overall efficiency becomes increasingly sensitive to parasitic transport penalties, particularly the geometric backscattering that severely degrades the forward throughput ratio at the channel inlet. Finally, Fig. 7 captures the intermediate phase of the geometric optimization landscape, where the thermodynamic benefits of artificially forcing boundary interactions through moderate tapering only marginally offset the macroscopic transport costs of the physical constriction.

Fig. 8 shows the efficiency for the high-affinity regime, with an intrinsic transmission probability of 0.045. In this high-permeability limit, the global macroscopic entropy generation is further minimized across the entire morphological spectrum. This pronounced reduction in global dissipation occurs because the elevated surface transmission probability ensures that the active species is rapidly extracted from the primary flow upon its initial boundary interactions. So, the permeating particles avoid the extensive accumulation of discrete entropic penalties that arise from repeated, momentum-erasing diffuse reflections within the channel bulk. The specific separation thermodynamic efficiency profile undergoes a definitive structural flattening, with the overall efficiency values compressed into a remarkably narrow band. The distinct, localized efficiency peak observed in the low-affinity systems entirely vanishes, replaced instead by a broad plateau of optimal performance that extends progressively towards weaker tapering ratios, approaching the uniform geometry limit ($\chi \rightarrow 1$). This behavior provides the final quantitative confirmation of the critical morphological transition postulated in the theoretical framework. Because the intrinsic permeation chemistry is inherently efficient at this upper limit, artificially imposing severe geometric constrictions fails to provide any necessary enhancement to the separation mechanics. Instead, strong tapering predominantly induces parasitic macroscopic transport penalties (i.e., severe inlet backscattering) that degrade the forward throughput ratio without yielding a corresponding gain in separation work. Finally, this figure shows that highly selective, high-affinity membranes favor uniform or weakly tapered channel architectures to mitigate irreversible transport losses and maximize macroscopic thermodynamic efficiency.

A comprehensive comparative analysis of Figs. 6–8 elucidates a fundamental morphological transition dictated entirely by the intrinsic surface affinity of the selective boundary. By tracking the evolution of the specific separation thermodynamic efficiency across the complete parametric space of P_{trans}, a systematic shift in optimal cascade design is observed. In the low-affinity regime (P_{trans}=0.015, Fig. 6), the η_{ST} profile is sharply non-monotonic, with a distinct optimal peak near $\chi \sim 0.65$. As the intrinsic transmission probability increases to 0.045 (Fig. 8), the distinct performance peak gradually broadens and dissolves into a flat plateau that extends decisively toward the uniform geometry limit ($\chi \rightarrow 1$).

This macroscopic transition is corroborated by the spatially resolved permeation fluxes detailed in Fig. 4. As the membrane affinity increases, the characteristic decay length of the exponential reaction-diffusion profile shortens drastically. This signifies that the majority of the permeating species is successfully extracted almost immediately upon entering the channel, effectively neutralizing the need for geometrically forced collision events deeper within the channel. So, as visualized in the morphological trajectories of Fig. 3, high-affinity systems do not require the severe spatial collision forcing that drives separation in low-affinity boundaries. Furthermore, the global thermodynamic budget mirrors this shifting dependence. Comparing the solid curves across the three efficiency figures reveals a progressive decline in the absolute magnitude of the global macroscopic entropy generation as permeability increases. Because the rapidly permeating particles in high-affinity systems are extracted at the inlet, they circumvent the heavy, cumulative entropic penalties associated with momentum-erasing diffuse boundary collisions deeper within the tapered conduit. In such optimized chemical regimes, imposing severe geometric constrictions (e.g., χ=0.25) becomes thermodynamically unfavorable. Severe dimensional reduction merely amplifies inlet backscattering and penalizes the forward throughput ratio without offering any compensatory gain in separation work. Finally, these combined metrics prove that the optimal geometric architecture is not static. Low-affinity membranes fundamentally demand moderate tapering to force interaction, whereas high-affinity boundaries strictly favor uniform geometries to mitigate parasitic macroscopic transport penalties.

It is important to contextualize the absolute magnitude of these efficiency optimizations. While the numerical variation in η_{ST} across the tapering spectrum may appear modest (typically manifesting as single-digit percentage shifts) this narrow operational band is intrinsically governed by the highly dissipative, chaotic nature of stochastic free-molecular flow. Single-stage Knudsen separation is fundamentally a low-yield process. However, because practical separation architectures rely on massive, multi-stage compounding cascades, a structural thermodynamic efficiency gain of merely 2–5% at the localized single-stage level scales exponentially. Over hundreds of sequential stages, this localized optimization translates into massive aggregate reductions in global entropy generation, external compression work, and required cascade footprint. Furthermore, while highly complex tortuous networks or asymmetric ratcheted pores might theoretically offer alternative active separation pathways, the continuous linear taper evaluated herein serves as the canonical physical baseline. It isolates the fundamental thermodynamic trade-off of broken spatial symmetry, formally establishing the theoretical limits of geometric collision forcing without the confounding transport variables introduced by complex fractal topologies.

Before concluding, it is necessary to acknowledge the theoretical limitations of the proposed framework. First, the thermodynamic derivations are predicated on the assumption of strictly diffuse boundary

interactions, effectively assuming a Tangential Momentum Accommodation Coefficient (TMAC) of unity. While this serves as the standard theoretical baseline for maximizing momentum erasure in Knudsen flow, realistic nanoporous boundaries frequently exhibit a finite specular reflection component. Because specular reflection conserves longitudinal momentum, a physical system with a TMAC of less than one would experience less severe discrete exergy destruction per collision, meaning the global macroscopic entropy generation limits established herein represent a worst-case thermodynamic upper bound. Second, the spatial integration of entropy generation formalized in Eq. 11 relies on a geometric approximation. By mathematically treating entropy production as a discrete, continuous penalty strictly inversely proportional to the local channel width, the proposed model successfully captures the dominant frictional penalty of macroscopic constriction. However, this approach inherently abstracts away the nuanced, higher-order thermodynamic costs associated with complex particle-surface interaction potentials, varied surface roughness topographies, and transient adsorption dwell times. Future iterations of this stochastic framework could incorporate variable accommodation coefficients and physical dwell times to map these non-ideal interfacial effects.

5. Conclusions

In this study, the non-equilibrium transport dynamics and macroscopic thermodynamic efficiency of a binary gas mixture traversing a tapered, semipermeable channel operating strictly within the Knudsen regime were investigated. It is important to note that the scope of this study is strictly bounded by the free-molecular assumption (Kn>>1). Consequently, the observed thermodynamic dependencies and geometric optimization rules are applicable only to highly rarefied flows or extreme nanoconfinement, wherein intermolecular scattering is entirely suppressed and the transport mechanics are governed purely by stochastic particle-boundary interactions. By computationally decoupling strictly ballistic spatial propagation from stochastic boundary interactions using a Lagrangian test particle Monte Carlo formalism, the microscopic trajectories governed by the underlying overdamped Langevin dynamics were successfully bridged with the macroscopic, ensemble-level concentration profiles described by the Fokker-Planck equation.

This unified framework allowed for the quantification of the thermodynamic irreversibility inherent in momentum erasure via diffuse boundary collisions. The baseline analysis demonstrated that geometric constriction in tapered channels induces significant macroscopic backscattering, which fundamentally impairs the forward throughput ratio. In the severe taper limit, forcing a finite flux through a severely choked exit necessitates a logarithmically divergent number of diffuse collisions, fundamentally destroying separation efficiency.

The introduction of selective membrane permeability breaks the spatial symmetry between the confined and permeating species, fundamentally transforming the uniform density profile into an exponentially decaying reaction-diffusion profile. This spatial extraction mechanism reveals a critical morphological transition dictated entirely by the intrinsic surface affinity of the active boundary. For low-affinity selective membranes, it was established that a moderate geometric constriction is fundamentally required to mechanically force wall collisions and artificially amplify the cumulative collision probability. This intermediate tapering profile optimally balances the separation work gain against the compounding irreversible entropic costs and parasitic macroscopic transport penalties, such as excessive inlet backscattering. On the other hand, as the intrinsic transmission probability of the membrane increases, the necessity for geometrically induced collision forcing diminishes, given that the vast majority of the permeating species is efficiently extracted near the channel inlet. Consequently, high-affinity membranes inherently favor more uniform or weakly tapered geometries.

By introducing the specific separation thermodynamic efficiency, the geometric performance of the channel was effectively decoupled from the specific membrane chemistry. This metric achieves this decoupling by decomposing the system's overall performance into its competing operational dependencies: it operates as a scalarized objective function that evaluates the targeted thermodynamic utility (the separation work gain) against a compound penalty index, consisting of the microscopic informational loss (cumulative entropy generation) and the macroscopic kinematic resistance (the backscattering probability), with all terms normalized by the intrinsic baseline transmission probability of the material.

Finally, this specific efficiency provides a unified, scale-invariant framework that explicitly links single-particle Knudsen statistics to the macroscopic geometric optimization of multi-stage separation cascades. The fundamental physical importance of this linkage lies in its ability to establish the theoretical bounds of rarefied gas separation. By mathematically proving that the geometric necessity of mechanical collision forcing is inversely proportional to the intrinsic material affinity, a thermodynamic proof is provided that no universal 'optimal' membrane pore shape can physically exist. Instead, the structural architecture itself must actively manage the dissipation of non-equilibrium concentration gradients. These findings confirm that the optimal geometric architecture is not static but must be dynamically tailored to the intrinsic chemical affinity of the boundary layer, ensuring that cascade design strictly adheres to the underlying thermodynamic limits of the system.

CRediT authorship contribution statement

Antonio F. Miguel: Writing – review & editing, Writing – original draft, Visualization, Validation, Methodology, Investigation, Formal analysis, Conceptualization.

Declaration of Competing Interest

The authors declare that they have no known competing financial interests or personal relationships that could have appeared to influence the work reported in this paper.

Acknowledges

The author gratefully acknowledges the financial support provided to the ICT through the multi-annual funding agreement with the Foundation for Science and Technology of Portugal (FCT), under project UID/0468

Data availability

No data was used for the research described in the article.

References

[1] F. Javadpour, H. Singh, A. Rabbani, M. Babaei, S. Enayati, Gas flow models of shale: a review, Energy Fuels 35 (2021) 2999–3010, https://doi.org/10.1021/acs.energyfuels.0c04381.
[2] Z.E. Sahin, A. Rahimalimamaghani, M. Gazzani, F. Gallucci, Gas permeation through carbon membranes: model development and experimental validation, Int. J. Hydrog. Energy 50 (2024) 561–581, https://doi.org/10.1016/j.ijhydene.2023.08.272.
[3] M. Barisik, A. Beskok, Scale effects in gas nano flows, Phys. Fluids 26 (2014) 052003, https://doi.org/10.1063/1.4874678.
[4] X.-J. Gu, R.W. Barber, B. John, D.R. Emerson, Non-equilibrium effects on flow past a circular cylinder in the slip and early transition regime, J. Fluid. Mech. 860 (2018) 654–681, https://doi.org/10.1017/jfm.2018.869.
[5] C. Corral-Casas, J. Li, M.K. Borg, L. Gibelli, Knudsen minimum disappearance in molecular-confined flows, J. Fluid. Mech. 945 (2022) A28, https://doi.org/10.1017/jfm.2022.563.
[6] R. Groll, S. Kunze, B. Besser, Correction of second-order slip condition for higher Knudsen numbers by approximation of free-molecular diffusion, Phys. Fluids 32 (2020) 092008, https://doi.org/10.1063/5.0021711.
[7] M.M. Kratzer, S.K. Bhatia, A.Y. Klimenko, On the increased interfacial resistance of hydrogen in carbon nanotube arrays and its effect on gas mixture separation, J. Appl. Phys. 135 (2024) 234301, https://doi.org/10.1063/5.0207999.

[8] H. Fan, M. Peng, I. Strauss, A. Mundstock, H. Meng, J. Caro, MOF-in-COF molecular sieving membrane for selective hydrogen separation, Nat. Commun. 12 (2021) 38, https://doi.org/10.1038/s41467-020-20298-7.
[9] L.P. Kholpanov, D.V. Potapov, G.A. Sulaberidze, V.A. Chuzhinov, On the calculation of a squared-off cascade for multicomponent isotope separation, Chem. Eng. Process. 37 (1998) 359–365.
[10] H. Darabi, A. Ettehad, F. Javadpour, K. Sepehrnoori, Gas flow in ultra-tight shale strata, J. Fluid. Mech. 710 (2012) 641–658, https://doi.org/10.1017/jfm.2012.424.
[11] I. Lunati, S.H. Lee, A dual-tube model for gas dynamics in fractured nanoporous shale formations, J. Fluid. Mech. 757 (2014) 943–971, https://doi.org/10.1017/jfm.2014.519.
[12] S. Eule, R. Friedrich, F. Jenko, Anomalous transport in a one-dimensional Lorentz gas model, J. Chem. Phys. 129 (2008) 174308, https://doi.org/10.1063/1.2953318.
[13] O. Eterigho-Ikelegbe, S.O. Bada, M.O. Daramola, Preparation and evaluation of nanocomposite sodalite/α-Al2O3 tubular membranes for H2/CO2 separation, Membranes 10 (2020) 312, https://doi.org/10.3390/membranes10110312.
[14] M.M. Kratzer, S.K. Bhatia, A.Y. Klimenko, Stochastic models of free-molecular nanopore flows, J. Chem. Phys. 158 (2023) 214101, https://doi.org/10.1063/5.0148289.
[15] J. Qian, H. Wu, F. Wang, A generalized Knudsen theory for gas transport with specular and diffuse reflections, Nat. Commun. 14 (2023) 7356, https://doi.org/10.1038/s41467-023-43104-6.
[16] S. Dutt, P. Apel, N. Lizunov, C. Notthoff, Q. Wen, C. Trautmann, et al., Shape of nanopores in track-etched polycarbonate membranes, J. Membr. Sci. 638 (2021) 119681, https://doi.org/10.1016/j.memsci.2021.119681.
[17] Y. Zhang, H. Han, S. Dou, X. Wu, J. Qiu, B. Nie, R. Wei, Diode characteristics of gas flow through conical nanochannels at atmospheric pressure, Phys. Fluids 36 (2024) 112016, https://doi.org/10.1063/5.0239419.
[18] H. Yu, Z. Tian, F. Yang, H. Li, Molecular dynamics simulation on the splitting of shear flow in nanochannels, AIP Adv. 11 (2021) 035017, https://doi.org/10.1063/5.0023159.
[19] V. Johny, S. Ghosh, Active solid-state nanopores: self-driven flows/chaos at the liquid–gas nanofluidic interface, Langmuir 39 (2023) 18889–18898, https://doi.org/10.1021/acs.langmuir.3c02776.
[20] S.R. de Groot, P. Mazur, Non-equilibrium thermodynamics, Dover Publications, 1984.
[21] D.J. Evans, E.G.D. Cohen, G.P. Morriss, Probability of second law violations in shearing steady states, Phys. Rev. Lett. 71 (1993) 2401.
[22] A.M. Berezhkovskii, S.M. Bezrukov, Fluctuation theorem for channel-facilitated membrane transport of interacting and noninteracting solutes, J. Phys. Chem. B 112 (2008) 6228–6232, https://doi.org/10.1021/jp075870i.
[23] U. Seifert, Stochastic thermodynamics, fluctuation theorems and molecular machines, Rep. Prog. Phys. 75 (2012) 126001, https://doi.org/10.1088/0034-4885/75/12/126001.
[24] D. Andrieux, P. Gaspard, Fluctuation theorem for transport in mesoscopic systems, J. Stat. Mech. (2006) P01011, https://doi.org/10.1088/1742-5468/2006/01/P0101.
[25] E.A. Mason, A.P. Malinauskas, Gas Transport in Porous Media: The Dusty-Gas Model, Elsevier, Amsterdam, 1983.
[26] W.J. Koros, C. Zhang, Materials for next-generation gas separation membranes, Nat. Mater. 16 (2017) 289–297, https://doi.org/10.1038/nmat4805.
[27] M. Knudsen, Die Gesetze der Molekularströmung und der inneren Reibungsströmung der Gase durch Röhren, Ann. Phys. 333 (1909) 75–130, https://doi.org/10.1002/andp.19093330106.
[28] K. Malek, M.-O. Coppens, Knudsen self- and Fickian diffusion in rough nanoporous media, J. Chem. Phys. 119 (2003) 2801–2811, https://doi.org/10.1063/1.1584652.
29] F. Celestini, F. Mortessagne, The cosine law at the atomic scale: toward realistic simulations of Knudsen diffusion, Phys. Rev. E 77 (2008) 021202, https://doi.org/10.1103/PhysRevE.77.021202.
[30] C. Heyde, Central limit theorem, in: Encyclopedia of Actuarial Science, 1, John Wiley & Sons, Ltd, USA, 2006.
[31] D.J. Evans, D.J. Searles, Equilibrium microstates which generate second law violating steady states, Phys. Rev. E 50 (1994) 1645, https://doi.org/10.1103/PhysRevE.50.1645.
[32] G. Gallavotti, E.G.D. Cohen, Dynamical ensembles in nonequilibrium statistical mechanics, Phys. Rev. Lett. 74 (1995) 2694, https://doi.org/10.1103/PhysRevLett.74.2694.
[33] G.E. Crooks, Entropy production fluctuation theorem and the nonequilibrium work relation for free energy differences, Phys. Rev. E 60 (1999) 2721, https://doi.org/10.1103/PhysRevE.60.2721.
[34] M. Matsumoto, T. Nishimura, Mersenne twister: a 623-dimensionally equidistributed uniform pseudo-random number generator, ACM Trans. Model. Comput. Simul. 8 (1998) 3, https://doi.org/10.1145/272991.27299.